Phys Chem Minerals (2001) 28: 399–412

ORIGINAL PAPER

R. J. Harrison · S. A. T. Redfern

Short- and long-range ordering in the ilmenite–hematite solid solution

Received: 25 May 2000 / Accepted: 12 January 2001

Abstract Magnetic and cation ordering in the ilmenite–hematite solid solution ($FeTiO_3$–Fe_2O_3) has been studied using in-situ high-temperature time-of-flight neutron powder diffraction. Synthetic samples containing 60 and 65% $FeTiO_3$ (ilm60 and ilm65, respectively) were heated under vacuum up to 1000 °C and their magnetic structure, crystal structure and cation distribution were determined via Rietveld refinement. The quenched starting materials display diffuse superlattice reflections, indicative of short-range cation order. The short-range ordered structure is interpreted with the aid of statistical simulations to be a fine-scale alternation of ordered and antiordered ilmenite-like twin domains, separated by hematite-like twin-domain boundaries (TDBs). Peak width analysis demonstrates that the twin domains have a pronounced shape anisotropy, with average lengths of 20 ± 1 and 60 ± 2 Å along the *c*-axis, and 100 ± 9 and 100 ± 4 Å along $[0\bar{1}1]$* in ilm60 and ilm65, respectively. Long-range order increases initially by a process of domain coarsening as the quenched samples are heated below the cation order-disorder temperature, T_{od}. The degree of order then decreases as they are heated through the transition. This leads to a kinetic relaxation behaviour, in which the observed rate of ordering is determined by the balance between the rate of coarsening and the rate of disordering within the domains. A phenomenological kinetic model is developed, which provides an excellent description of the observed behaviour in both samples. Once long-range order has been established, the equilibrium degree of order as a function of temperature is well described by a modified Bragg-Williams model, yielding values of $T_{od} = 830 \pm 20$ °C and 911 ± 20 °C for ilm60 and ilm65, respectively. Analysis of the magnetic scattering and spontaneous strain demonstrates that short-range magnetic order remains at temperatures well above the bulk Curie temperatures ($T_c = 178$ °C and 143 °C in ilm60 and ilm65, respectively). This indicates significant magnetic heterogeneity in the samples, which may be related to the presence of a high density of Fe-enriched TDBs in the quenched material.

R. J. Harrison (✉)
Institut für Mineralogie, Universität Münster,
Corrensstrasse 24, 48149 Münster, Germany
e-mail: harrisr@nwz.uni-muenster.de

S. A. T. Redfern
Department of Earth Sciences, University of Cambridge,
Downing Street, Cambridge CB2 3EQ, UK
e-mail: satr@cam.ac.uk

Introduction

Members of the ilmenite–hematite solid solution commonly occur as accessory minerals in igneous and metamorphic rocks, and are significant bearers of natural remanent magnetization. Their thermodynamic and magnetic properties are influenced by three processes (Fig. 1): (1) cation ordering in ilmenite-rich compositions; (2) exsolution in intermediate compositions; and (3) magnetic ordering across the entire solid solution. The cation ordering phase transition occurs at a critical temperature, T_{od}, and is caused by partitioning of Fe and Ti onto alternating (001) octahedral layers (Harrison et al. 2000a). The loss of symmetry on cooling through T_{od} leads to the formation of fine-scale twin domains separated by meandering twin-domain boundaries (TDBs). The TDBs are thought to be responsible for the unusual magnetic properties observed in intermediate compositions, such as the tendency to acquire self-reversed thermoremanent magnetization (Nord and Lawson 1989, 1992; Hoffman 1992).

There is compelling evidence to support a correlation between self-reversal and the presence of TDBs (Harrison 2000). However, some aspects of the self-reversal mechanism remain the subject of debate. A fundamental requirement of the model is that the TDBs are Fe-enriched and therefore capable of acquiring a remanent magnetization at higher temperatures than the domains themselves. This Fe-enrichment hypothesis has yet to be confirmed by direct chemical analysis, and the width and

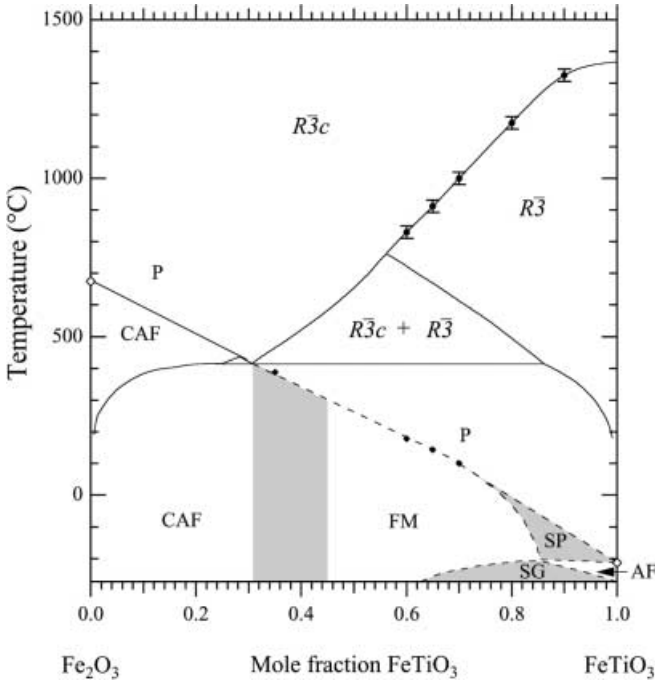

Fig. 1 Summary of phase relations in the ilmenite–hematite solid solution: $R\bar{3}c$ cation disordered; $R\bar{3}$ cation ordered; *P* paramagnetic; *CAF* canted antiferromagnetic; *FM* ferrimagnetic; *AF* antiferromagnetic; *SP* superparamagnetic; *SG* spin glass. *Closed circles* are T_{od} for the $R\bar{3}c$ to $R\bar{3}$ phase transition (Harrison et al. 2000a; this study). *Closed diamonds* show T_c for stoichiometric ilm35, ilm60, ilm65 and ilm70. End-member T_c's and SP, SG and AF fields from Ishikawa et al. (1985). Miscibility gap determined by Ghiorso (1997). Boundary between CAF and FM depends on thermal history (represented by *broad shaded region*). *Other lines* are guides to the eye

degree of enrichment of the TDBs is unknown. Investigation of Fe-enrichment using conventional magnetic measurements is difficult since the TDBs are antiferromagnetic with a weak parasitic moment and their signal is swamped by that of the ferrimagnetic domains. Investigation using neutron diffraction is potentially more useful because magnetic scattering is proportional to the sublattice magnetization rather than the net magnetization, so the signal from antiferromagnetic and ferrimagnetic regions is similar. Below T_{od}, TDBs are a metastable feature of the structure and disappear over time due to twin-domain coarsening. Although the rate of coarsening in the late stages of ordering is known (Nord and Lawson 1989), the rate of formation and coarsening of twin domains during rapid cooling is less well characterised. This is an important factor in assessing the role of TDBs in the acquisition of self-reversed thermoremanent magnetization in rapidly cooled andesitic pumices (Uyeda 1958).

To address some of these issues we have performed an in-situ neutron diffraction study of cation ordering in ilm60 and ilm65. In contrast to more ilmenite-rich samples, which acquire a high degree of long-range cation order on quenching from above T_{od}, quenched intermediate samples are expected to have only short-range cation order and a correspondingly high density of TDBs. The temperature dependence of the sublattice magnetization is determined from the intensity of magnetic reflections. The time-temperature evolution of the twin domains is followed via the width and integrated intensity of cation ordering superlattice reflections, while the average structure is determined via Rietveld refinement. We begin by describing the experimental results and provide a qualitative interpretation of the observations. Then we use a combination of thermodynamic and kinetic models to provide a quantitative description of the observed behaviour. Finally, we discuss the possible implications of the results to self-reversal in natural material.

Crystal and magnetic structure

Hematite has the corundum structure with space group $R\bar{3}c$. The oxygens form a distorted hexagonal close-packed arrangement and the Fe^{3+} cations occupy two thirds of the octahedral sites, forming symmetrically equivalent layers parallel to (001) (Fig. 2a). Ilmenite adopts a related structure with space group $R\bar{3}$, with Fe^{2+} and Ti cations partitioned onto alternating A and B layers (Fig. 2b). The solid solution is formed via the coupled substitution $2Fe^{3+} = Fe^{2+} + Ti^{4+}$. Above T_{od}, cations are randomly distributed and the structure has symmetry $R\bar{3}c$. Below T_{od}, Fe^{2+} and Ti partition onto the A and B layers, reducing the symmetry to $R\bar{3}$ and leading to the formation of twin domains (Nord and Lawson 1989). Adjacent domains are related to each other by 180° rotation about the *a*-axis and have an antiphase relationship with respect to their Fe–Ti distribution (i.e. an Fe-rich layer becomes a Ti-rich layer on crossing the TDB and vice versa).

Hematite has a canted antiferromagnetic structure. The antiparallel magnetic sublattices coincide with the A and B cation layers (Fig. 2a). The sublattice spins lie within the basal plane but are rotated by a small angle about [001], producing a weak parasitic magnetic moment (Dzyaloshinsky 1958). The disordered solid solution has the same antiferromagnetic structure as hematite, since Fe is equally distributed over the (001) layers and the A and B sublattice magnetizations are equal. The ordered solid solution is ferrimagnetic, since there are unequal amounts of Fe on the A and B sublattices. Ferrimagnetic ordering is disrupted by a spin glass transition at low temperatures in ilmenite-rich compositions (Ishikawa et al. 1985). Ilmenite itself has an antiferromagnetic structure with spins parallel to [001] (Fig. 2b).

Experimental procedures

Sample synthesis

The samples were synthesised from the oxides Fe_2O_3 and TiO_2 under controlled oxygen fugacity. A series of preliminary experiments were performed to determine the oxygen fugacity required to

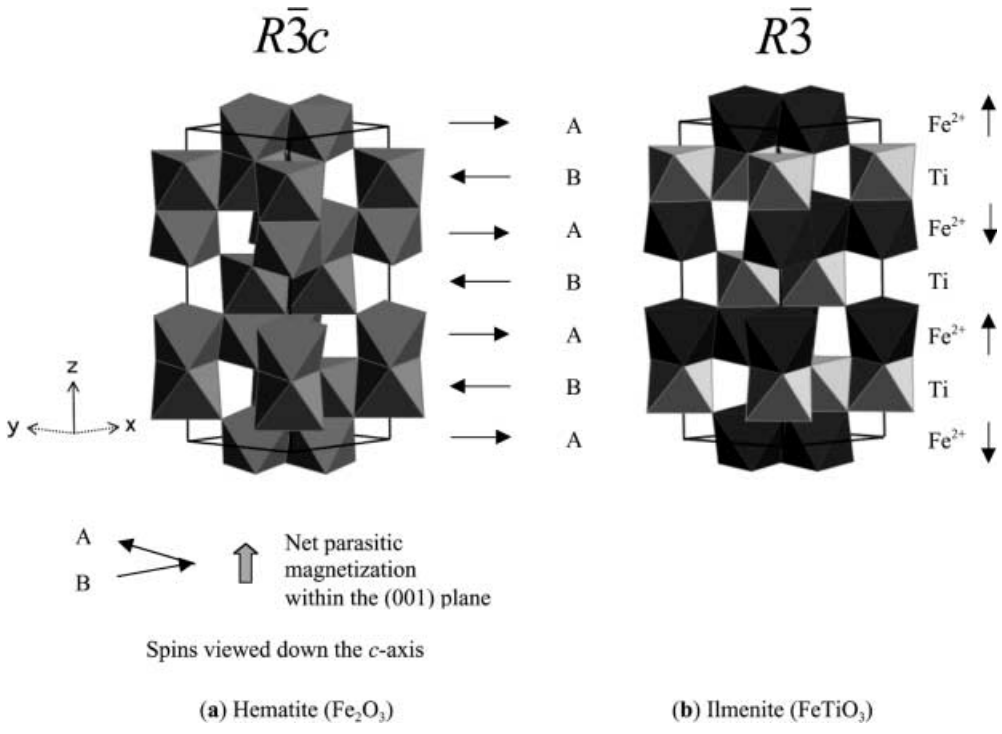

Fig. 2a, b Crystal and magnetic structure of **a** hematite (Fe_2O_3) and **b** ilmenite ($FeTiO_3$)

produce stoichiometric material, according to the method of Harrison et al. (2000a). The main synthesis experiments were performed by annealing several pressed pellets of the stoichiometric oxide mix for 24 h under the conditions given in Table 1. After quenching into water, a small amount from each pellet was ground with Si and examined using XRD over the range $22° < 2\theta < 89°$. The peak positions were determined by peak fitting and then corrected using a cubic spline fit to the six observable Si peaks. The lattice parameters (Table 1) were determined using the least-squares program UnitCell (Holland and Redfern 1997). Good agreement was observed between the unit-cell volumes of the synthetic samples and the calibration given by Brown et al. (1993). After XRD analysis, the samples were reground under acetone, pressed into pellets and annealed for a further 24 h under the same conditions. The final product was a stack of sintered pellets of 13 mm diameter and between 30 and 40 mm height for each bulk composition.

The magnetic properties of the starting materials were determined from the temperature dependence of magnetic susceptibility, according to the method of Harrison and Putnis (1999). The ilm60 sample was antiferromagnetic with Curie temperature $T_c = 178$ °C, while the ilm65 sample was weakly ferrimagnetic with $T_c = 143$ °C.

Neutron diffraction procedures

The neutron powder diffraction data were collected using the ROTAX time-of-flight diffractometer at the ISIS spallation neutron source (Rutherford Appleton Laboratory, UK). Diffracted intensity was measured using two fixed-angle banks of detectors located at scattering angles of 30 and 90° 2θ. Samples were loaded into standard vanadium cans and placed into a vanadium-element resistance furnace. The furnace was evacuated to a pressure of 4×10^{-5} mbar to prevent both the heating elements and the sample from oxidising during the experiment. No evidence of either oxidation or reduction of the sample was detected. Temperature was controlled and monitored using two type-K thermocouples placed approximately 2 cm above and below the sample pellet stack. The sample was left to thermally equilibrate for 5 min at each temperature. Neutron data were then acquired over a period of 1–2 h.

Structure refinements were performed only on data collected at temperatures of 200 °C and above to avoid any contribution from magnetic scattering. The crystal structures were refined assuming stoichiometric total site occupancies using the GSAS Rietveld refinement software (Larson and Von Dreele 1994). The background was modelled using a sixth-order Chebyshev polynomial. The crystallographic variables were the unit-cell parameters (a and c), the z-coordinates of the two cation sites (z_A and z_B), the x-, y- and z-coordinates of the oxygen atom (x_o, y_o and z_o), the A-site Ti occupancy (X_{Ti}^{A}), and the isotropic cation and oxygen displacement parameters (U_c and U_o). Peak-shape parameters and a correction parameter for the wavelength-specific absorption of neutrons by the sample were also refined. The experimental details of the structure refinements are shown in Table 2 and the results are listed in Table 3.

It was not possible to refine the crystal and magnetic structures simultaneously below 200 °C due to the superposition of nuclear and magnetic superlattice peaks with very different widths. Therefore only the cell parameters were determined at these temperatures.

Table 1 Synthesis conditions for ilmenite–hematite starting material

Composition (x)	Temperature (°C)	Volume ratio (CO_2/CO)	f_{O2}[a]
0.6	1300	0.993	−5.4
0.65	1300	0.992	−5.5

[a] Oxygen fugacity determined from tabulated values in Deines et al. (1974)

Results

Magnetic ordering

Neutron diffraction patterns for all temperatures and compositions studied are shown in Fig. 3. The

Table 2 Experimental and refinement details

Instrumental	
Diffractometer	ROTAX (neutron time-of-flight powder diffractometer)
Moderator	95 K methane
Incident flight path	14–16 m (variable)
Scattered flight path	0.5–1.6 m (variable)
Total flight path	14.5–17.6 m
Data range	0.4–5.2 Å
Time window	1–20 ms
Instrumental resolution $\delta d/d$	3.5×10^{-3}
Detectors:	2 linear position sensitive 6-Li glass scintilators
Refinement	
Space group	$R\bar{3}$ (below T_{od}) and $R\bar{3}c$ (above T_{od})
Z	6
Unit-cell refinement	Whole pattern
Observations	3306
Refined parameters	
Structural	8
Profile	6
Background	6 Chebychev polynomials of the first kind
Cell	2
Constraints	
Strict (site = 1)	TiA = FeA = TiB = FeB
Strict (equal Uiso)	TiA + FeA, TiB + FeB
Thermal parameters	All atoms isotropic
Agreement factors	See Table 3

measurements start at room temperature with the sample as quenched from 1300 °C. The $(1\bar{1}2)$ reflection with $d \approx 3.7$ Å is a fundamental reflection of the crystal structure. The $(0\bar{1}1)$ and (003) reflections with $d \approx 4.2$ Å and $d \approx 4.6$ Å are superlattice reflections, which appear only as a consequence of ordering. Both magnetic and nuclear scattering contribute to the superlattice intensity below 200 °C. The magnetic component is removed by heating to above the Curie temperature, T_c, whereas the nuclear component is expected to remain constant over this temperature range. This allows the two components to be easily separated.

The diffraction patterns have been fitted between $d = 3$ Å and $d = 10$ Å with five Gaussian peaks: one to describe the $(1\bar{1}2)$ fundamental reflection, two to describe the nuclear component of the superlattice reflections, and two to describe the magnetic component. The two nuclear peaks were determined first by fitting to the diffraction patterns collected at 200 °C. The height and width of these peaks were then held constant in the fits below 200 °C. The intensity of the magnetic peaks is proportional to $(M_A + M_B)^2$, where M_A and M_B are the magnetizations of the A and B sublattices (Shirane et al. 1959, 1962). The square root of the integrated magnetic intensity shows unusual behaviour in both samples (Fig. 4). Instead of decreasing smoothly to zero as T_c is approached, the curves show an inflection point close to the expected T_c (178 and 143 °C for ilm60 and ilm65, respectively) and significant scattering intensity up to 200 °C (where it is constrained to be zero by the fitting procedure). Evidence that magnetic scattering intensity remains at temperatures greater than 200 °C will be presented in the following sections. These observations indicate significant magnetic heterogeneity in the samples.

Cation ordering

Diffuse superlattice peaks due to cation ordering are observed above 200 °C (Fig. 3). The degree of cation order is described by the order parameter, Q, defined as:

$$Q = \frac{\left(X_{\mathrm{Ti}}^{\mathrm{B}} - X_{\mathrm{Ti}}^{\mathrm{A}}\right)}{\left(X_{\mathrm{Ti}}^{\mathrm{B}} + X_{\mathrm{Ti}}^{\mathrm{A}}\right)} \quad , \tag{1}$$

where X_i^j is the occupancy of i-type cations on j-type layers. The order parameter takes a value of $Q = 0$ in the fully disordered state and $Q = \pm 1$ in the fully ordered state. Positive and negative values of Q correspond to the degenerate ordered and antiordered states (i.e. the two alternative twin domains). Variations in Q throughout the crystal can be described in terms of Fourier components (Marais and Salje 1991):

$$Q(\mathbf{r}) = \sum_{\mathbf{k}} Q_{\mathbf{k}}\, \mathrm{e}^{i\mathbf{k}\cdot\mathbf{r}} \quad , \tag{2}$$

where $\mathbf{r}$ is distance and $\mathbf{k}$ is a wave vector. The intensity of a superlattice reflection at a given point in $\mathbf{k}$-space is given by the Fourier transformation:

$$I(\mathbf{k}) \propto \int \langle Q(\mathbf{r})Q(\mathbf{r}')\rangle \exp[i\mathbf{k}\cdot(\mathbf{r}-\mathbf{r}')]\mathrm{d}\mathbf{r}\,\mathrm{d}\mathbf{r}' \propto \langle Q_{\mathbf{k}}^2\rangle \quad . \tag{3}$$

The degree of long-range order is given by the $\mathbf{k} = 0$ component, whereas the degree of short-range order is given by the integrated intensity:

$$\sigma^2 \propto \int_{\mathbf{k}>0} I(\mathbf{k})\mathrm{d}\mathbf{k} \tag{4}$$

In other words, the width of a superlattice reflection gives a measure of the wavelength with which the order parameter fluctuates from positive to negative (i.e. the size of the twin domains), while the integrated intensity gives a measure of the amplitude of the fluctuations (i.e. the degree of order within the domains).

Large changes in the width and intensity of the superlattice reflections occur as the samples are heated and cooled through T_{od} (Fig. 3). These changes were quantified by fitting the diffraction patterns between $d = 3$ Å and $d = 10$ Å with three Gaussian peaks and a cubic polynomial background. The fit was performed over a wide range of d-spacings so that the diffuse peaks and the background could be easily separated. The temperature dependence of the peak widths (FWHM) is shown in Fig. 5. The dashed line shows the width of the $(1\bar{1}2)$ fundamental reflection, which gives an indication of the intrinsic broadening due to instrumental effects, crystallite size and strain. The broadening of the superlattice reflections is an order of magnitude greater, and is directly related to fluctuations in Q (Eq. 3). The main

Table 3 Structure refinements of ilmenite–hematite samples as a function of temperature and composition

T (°C)	a (Å)	c (Å)	X_{Ti}^{A}	Q	z_A	z_B	x_o	y_o	z_o	U_c(×100)	U_o(×100)
ilm60											
31	5.06740(13)	13.9139(6)									
50	5.06803(13)	13.9143(7)									
76	5.06914(12)	13.9158(6)									
102	5.07056(9)	13.9179(4)									
124	5.07246(10)	13.9201(5)									
164	5.07590(9)	13.9227(4)									
182	5.07693(9)	13.9237(1)									
203	5.07894(8)	13.9269(4)	0.180(3)	0.400(9)	0.35510(30)	0.14315(51)	0.3122(3)	0.0109(5)	0.2481(2)	1.125(32)	0.994(32)
298	5.08450(8)	13.9353(4)	0.184(3)	0.387(6)	0.35526(31)	0.14323(52)	0.3120(3)	0.0110(5)	0.2481(2)	1.222(33)	1.097(33)
399	5.09101(9)	13.9543(4)	0.166(3)	0.447(9)	0.35554(30)	0.14257(55)	0.3118(3)	0.0112(5)	0.2477(2)	1.53(4)	1.30(4)
498	5.09641(10)	13.9695(5)	0.127(2)	0.577(6)	0.35561(25)	0.14129(57)	0.3117(4)	0.0116(5)	0.2472(2)	1.72(5)	1.49(5)
506	5.09689(10)	13.9709(5)	0.105(2)	0.650(6)	0.35564(22)	0.14116(55)	0.3112(3)	0.0109(5)	0.2470(2)	1.69(5)	1.56(4)
549	5.10042(9)	13.9775(5)	0.097(2)	0.677(6)	0.35539(20)	0.14073(52)	0.3113(3)	0.0106(5)	0.2471(2)	1.79(4)	1.67(4)
598	5.10401(8)	13.9829(4)	0.089(2)	0.703(6)	0.35567(17)	0.14134(48)	0.3115(3)	0.0104(4)	0.2472(1)	1.82(4)	1.79(4)
647	5.10777(7)	13.9886(4)	0.092(2)	0.693(6)	0.35544(16)	0.14074(45)	0.3114(3)	0.0101(4)	0.2472(1)	1.89(4)	1.88(4)
697	5.11145(7)	13.9938(4)	0.108(2)	0.640(6)	0.35558(18)	0.14105(46)	0.3114(3)	0.0096(4)	0.2476(1)	2.01(4)	2.02(4)
721	5.11310(8)	13.9964(4)	0.123(2)	0.590(6)	0.35566(21)	0.14131(48)	0.3111(3)	0.0089(5)	0.2475(2)	2.08(4)	2.09(4)
745	5.11492(8)	13.9982(4)	0.139(2)	0.537(6)	0.35575(25)	0.14154(53)	0.3111(3)	0.0090(5)	0.2479(2)	2.16(4)	2.12(4)
769	5.11667(8)	14.0008(4)	0.161(2)	0.463(6)	0.35593(29)	0.14202(56)	0.3105(4)	0.0077(6)	0.2480(2)	2.17(5)	2.14(4)
793	5.11842(8)	14.0031(4)	0.192(3)	0.360(9)	0.35560(40)	0.14160(60)	0.3103(4)	0.0071(7)	0.2484(3)	2.25(5)	2.22(5)
818	5.12049(8)	14.0057(4)	0.3	0	0.35678(9)	0.14322(9)	0.3066(2)	0	0.25	2.93(4)	2.91(4)
844	5.12187(8)	14.0077(4)	0.3	0	0.35676(7)	0.14324(7)	0.3061(2)	0	0.25	2.35(5)	2.30(4)
921	5.12710(8)	14.0198(4)	0.3	0	0.35693(7)	0.14307(7)	0.3062(2)	0	0.25	2.52(5)	2.42(5)
999	5.13219(8)	14.0326(4)	0.3	0	0.35698(7)	0.14302(7)	0.3059(2)	0	0.25	2.65(5)	2.52(5)
795	5.11880(9)	14.0020(5)	0.198(3)	0.340(9)	0.35550(40)	0.14140(70)	0.3101(5)	0.0071(8)	0.2482(3)	2.70(4)	2.68(4)
594	5.10615(9)	13.9817(4)	0.065(2)	0.783(6)	0.35552(17)	0.14078(55)	0.3116(3)	0.0103(4)	0.2473(2)	2.177(31)	2.264(31)
392	5.09407(8)	13.9592(4)	0.035(2)	0.883(6)	0.35525(13)	0.14056(53)	0.3123(3)	0.0119(4)	0.2473(1)	1.753(27)	1.807(27)
203	5.08205(8)	13.9390(4)	0.028(1)	0.907(3)	0.35505(12)	0.14086(51)	0.3126(3)	0.0124(3)	0.2472(1)	1.406(24)	1.500(24)
48	5.07033(10)	13.9256(5)									
ilm65											
25	5.06972(11)	13.9202(6)									
59	5.07093(11)	13.9228(6)									
90	5.07248(11)	13.9248(6)									
117	5.07445(11)	13.9278(5)									
123	5.07598(10)	13.9302(5)									
144	5.07691(11)	13.9309(5)									
170	5.07852(11)	13.9334(6)									
191	5.08021(11)	13.9352(6)									
209	5.08175(10)	13.9383(5)	0.109(2)	0.665(6)	0.35479(19)	0.14073(56)	0.3128(3)	0.0132(4)	0.2472(1)	1.13(4)	1.01(4)
301	5.08755(10)	13.9485(5)	0.111(2)	0.658(6)	0.35485(19)	0.14040(57)	0.3127(3)	0.0134(4)	0.2471(1)	1.29(4)	1.15(4)
398	5.09392(10)	13.9672(5)	0.088(2)	0.729(6)	0.35527(19)	0.13950(66)	0.3126(3)	0.0136(4)	0.2469(1)	1.52(5)	1.37(5)
497	5.09968(11)	13.9803(5)	0.080(2)	0.754(6)	0.35536(18)	0.13810(67)	0.3123(3)	0.0132(4)	0.2467(1)	1.72(5)	1.58(5)
597	5.10668(10)	13.9928(5)	0.075(2)	0.769(6)	0.35556(17)	0.13907(65)	0.3123(3)	0.0123(4)	0.2467(1)	1.83(5)	1.85(5)
697	5.11451(9)	14.0061(4)	0.077(2)	0.763(6)	0.35585(16)	0.13954(63)	0.3126(3)	0.0123(4)	0.2470(1)	2.06(5)	2.07(5)
745	5.11897(8)	14.0135(4)	0.089(2)	0.726(6)	0.35564(16)	0.13904(57)	0.3123(3)	0.0119(4)	0.2474(1)	2.13(5)	2.15(4)
794	5.12327(8)	14.0202(4)	0.114(2)	0.649(6)	0.35588(19)	0.14024(57)	0.3121(3)	0.0114(4)	0.2475(2)	2.25(5)	2.27(5)
818	5.12539(8)	14.0237(4)	0.132(2)	0.594(6)	0.35571(21)	0.13982(56)	0.3119(3)	0.0110(4)	0.2477(2)	2.28(5)	2.28(5)
843	5.12732(8)	14.0255(4)	0.156(2)	0.520(6)	0.35590(25)	0.14010(59)	0.3116(3)	0.0104(5)	0.2479(2)	2.36(5)	2.34(5)
868	5.12940(9)	14.0271(4)	0.190(3)	0.415(9)	0.35576(33)	0.14063(62)	0.3111(4)	0.0097(6)	0.2481(2)	2.39(5)	2.32(5)

Table 3 (Continued)

T (°C)	a (Å)	c (Å)	X^{A}_{Ti}	Q	z_A	z_B	x_o	y_o	z_o	U_c(×100)	U_o(×100)
893	5.13122(9)	14.0301(5)	0.233(4)	0.283(12)	0.35550(40)	0.14060(70)	0.3113(4)	0.0101(7)	0.2486(3)	2.50(6)	2.37(5)
918	5.13336(9)	14.0327(5)	0.325(0)	0	0.35716(8)	0.14284(8)	0.3062(2)	0	0.25	2.55(6)	2.42(5)
945	5.13530(9)	14.0372(5)	0.325(0)	0	0.35715(8)	0.14285(8)	0.3060(2)	0	0.25	2.60(6)	2.47(5)
994	5.13927(9)	14.0457(5)	0.325(0)	0	0.35726(8)	0.14274(8)	0.3058(2)	0	0.25	2.61(6)	2.45(6)
893	5.13220(9)	14.0317(5)	0.229(4)	0.295(12)	0.35590(50)	0.14120(70)	0.3109(4)	0.0098(7)	0.2485(3)	2.42(6)	2.28(5)
793	5.12512(8)	14.0236(4)	0.108(2)	0.668(6)	0.35591(19)	0.13993(60)	0.3118(3)	0.0112(4)	0.2474(2)	2.19(5)	2.18(5)
592	5.11249(8)	14.0019(4)	0.041(1)	0.874(3)	0.35552(12)	0.13785(62)	0.3129(3)	0.0134(3)	0.2469(1)	1.71(4)	1.81(4)

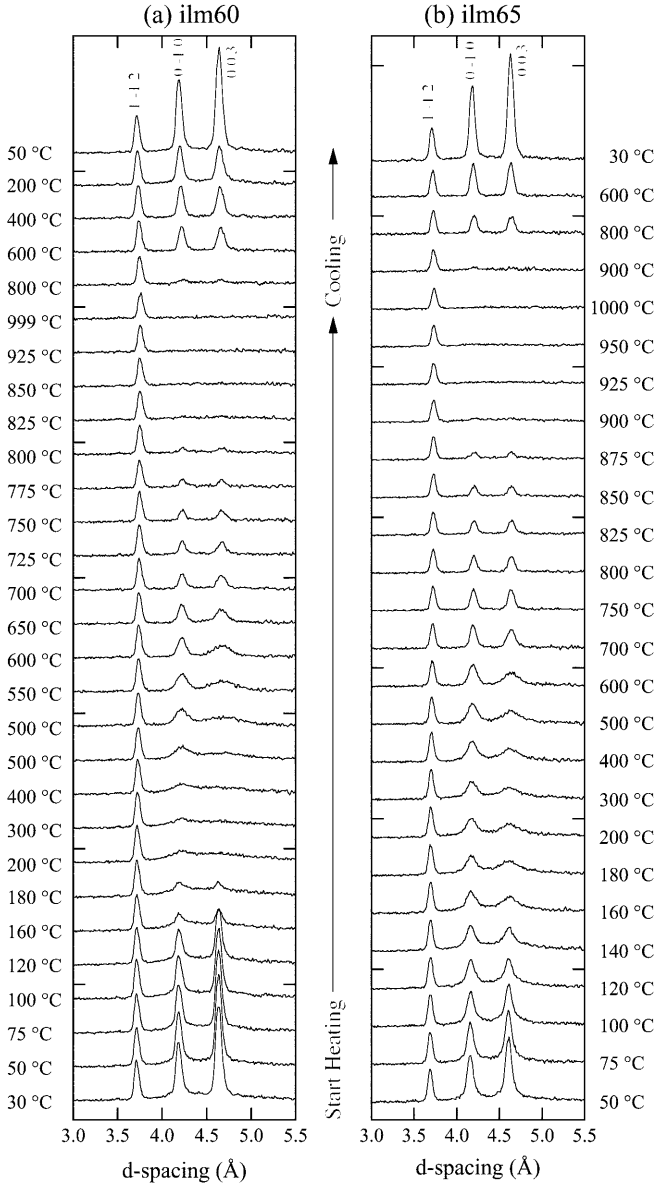

Fig. 3a, b Neutron diffraction profiles of the $(1\bar{1}2)$ fundamental reflection ($d \approx 3.7$ Å) and the $(0\bar{1}1)$ and (003) superlattice reflections ($d \approx 4.2$ Å and $d \approx 4.6$ Å, respectively), as a function of temperature for **a** ilm60 and **b** ilm65

source of fluctuations is the twin domains which form on quenching through T_{od}. If we picture the short-range ordered structure as a simple alternation of ordered and antiordered domains, the domain size can be estimated using the Scherrer formula (Delhez et al. 1995):

$$\langle D \rangle_{[hkl]^*} = \frac{d_{hkl}^2}{1.06\Gamma_{hkl}} \quad , \tag{5}$$

where $\langle D \rangle_{[hkl]^*}$ is the average linear dimension of the domains measured parallel to the reciprocal lattice vector $[hkl]^*$, d_{hkl} is the d-spacing of the hkl reflection, and Γ_{hkl} is the FWHM. The factor 1.06 relates the FWHM of a Gaussian peak to its integral width (i.e. the width of a rectangle having the same height and area as the peak).

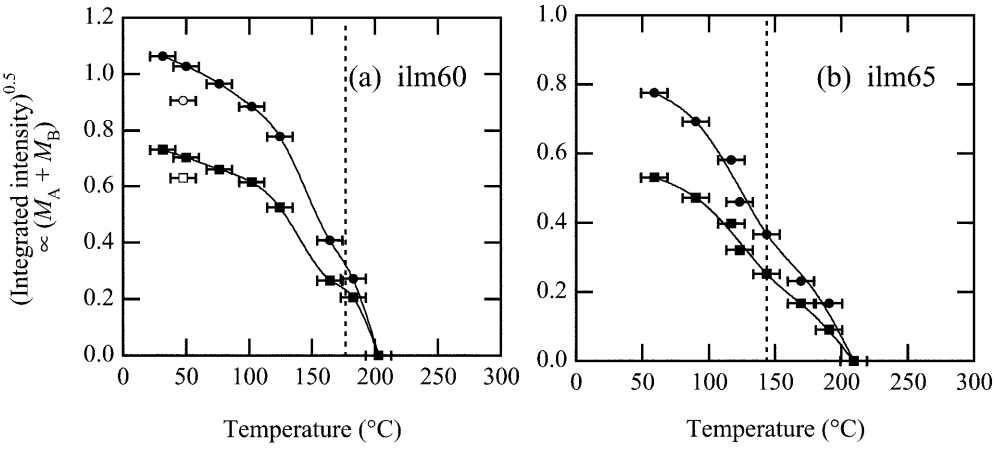

Fig. 4a, b Square root of the integrated magnetic intensity of the $(0\bar{1}1)$ (*squares*) and (003) (*circles*) superlattice reflections as a function of temperature for **a** ilm60 and **b** ilm65. *Open symbols* in **a** show the cooling data. *Solid lines* are guides to the eye. *Dashed lines* show the Curie temperatures determined via magnetic susceptibility measurements

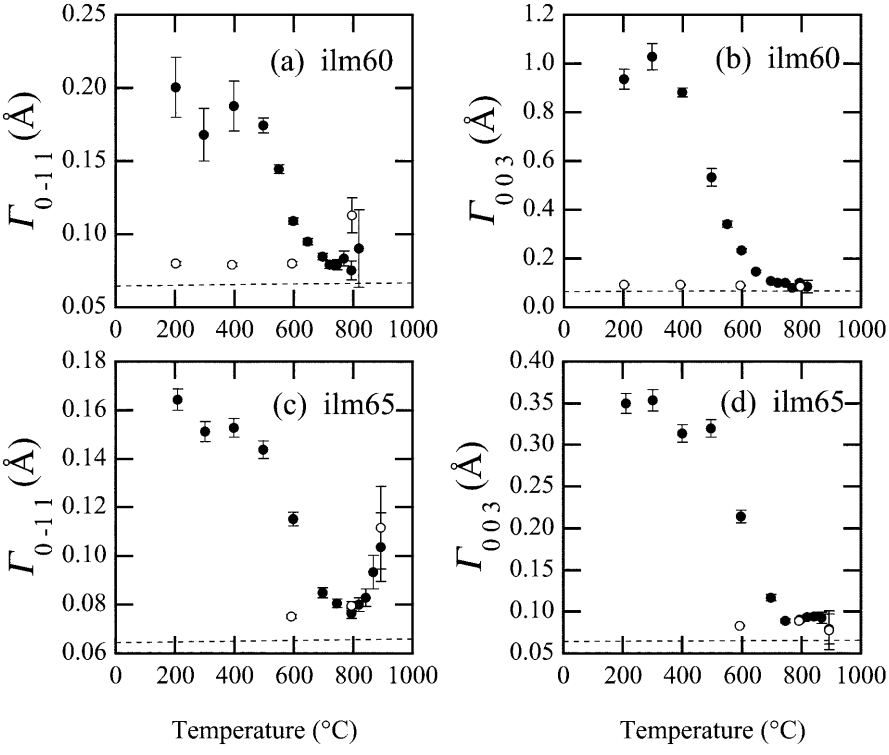

Fig. 5a–d FWHM of the $(0\bar{1}1)$ and (003) superlattice reflections as a function of temperature for ilm60 (**a** and **b**) and ilm65 (**c** and **d**). *Dashed line* is the FWHM of the $(1\bar{1}2)$ fundamental reflection. *Open symbols* show the cooling data

An approximate correction for instrumental broadening can be made by subtracting the width of the fundamental reflection (Delhez et al. 1995):

$$\Gamma^2_{\text{corrected}} = \Gamma^2_{hkl} - \Gamma^2_{1\bar{1}2} \quad . \tag{6}$$

Domains in the quenched starting material are extremely small and show a pronounced anisotropy. Equation (5) yields $\langle D\rangle_{[003]^*} = 20 \pm 1$ Å and $\langle D\rangle_{[0\bar{1}1]^*} = 100 \pm 9$ Å for ilm60. Corresponding values of 60 ± 2 Å and 100 ± 4 Å are obtained for ilm65. Above 400 °C the peak widths decrease rapidly due to domain coarsening. The peak widths continue to decrease until a temperature approximately 100 °C below T_{od}, at which point they are close to the intrinsic resolution and Eq. (5) yields $\langle D\rangle_{[003]^*} \approx \langle D\rangle_{[0\bar{1}1]^*} \approx$ 400–500 Å. Between ($T_{\text{od}} - 100$) and T_{od} the peak widths remain constant or increase (e.g. Fig. 5c). This is most likely due to the development of order parameter fluctuations within individual domains as the critical temperature is approached.

On cooling, the superlattice reflections reappear with widths close to the instrumental resolution (open circles in Fig. 5). Significant broadening is observed close to T_{od} due to the presence of critical fluctuations, but these are suppressed at temperatures below T_{od}. We find $\langle D\rangle_{[003]^*} \approx 311 \pm 6$ Å and $\langle D\rangle_{[0\bar{1}1]^*} \approx 373 \pm 9$ Å for ilm60 at 200 °C. Corresponding values of 403 ± 6 Å and 458 ± 5 Å are obtained for ilm65 at 600 °C. The large domain size is attributed to the fact that both samples were annealed at temperatures below T_{od} for several hours on cooling.

The temperature dependence of the integrated superlattice intensity is shown in Fig. 6. The superlattice intensities have been normalised relative to the intensity of the $(1\bar{1}2)$ fundamental reflection, to account for the effect of increased thermal vibration at high temperatures. In all cases, the intensity observed at 200 °C in the quenched starting material is greater than that displayed at 300 °C. This is most likely explained by the presence of diffuse magnetic intensity contributing to the measurement at 200 °C, which is removed on heating to 300 °C. The dashed lines show the variation in intensity predicted by the relationship $I \propto Q_{eq}^2$, where Q_{eq} is the equilibrium degree of order for a given temperature (see next section). Ideally, the presence of twin domains has no effect on the integrated intensity of the superlattice reflections, and all data points should lie close to the dashed line. Departures from this classical behaviour occur at low temperatures due to a combination of kinetic and short-range ordering effects. All reflections follow the predicted behaviour closely at high temperatures (and on cooling) once the domains have coarsened and long-range order is established.

Equilibrium cation distribution

The long-range order parameter, Q, has been calculated from Eq. (1) using values of X_i^J extracted from the Rietveld refinements (Table 2; Fig. 7). The peak widths were assumed to vary smoothly as a function of

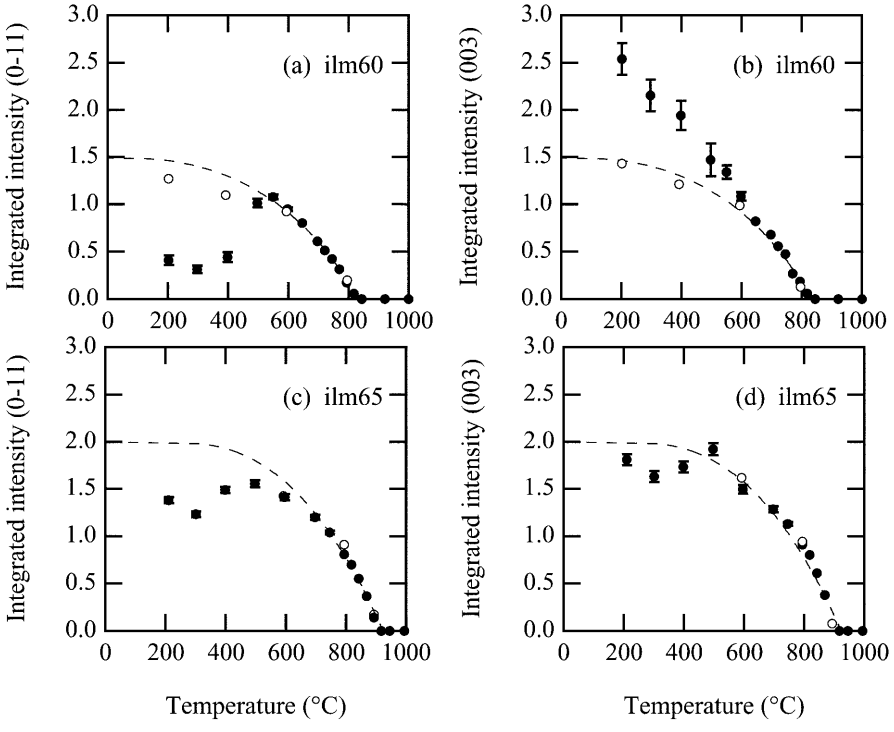

Fig. 6a–d Integrated intensity of the $(0\bar{1}1)$ and (003) superlattice reflections as a function of temperature for ilm60 (**a** and **b**) and ilm65 (**c** and **d**). *Dashed line* is the ideal variation in intensity according to the relationship $I \propto Q_{eq}^2$. *Open symbols* show the cooling data

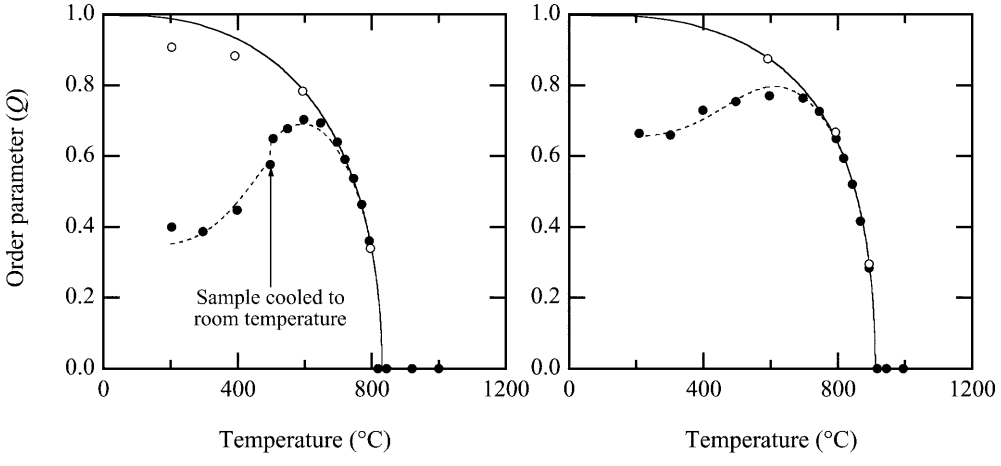

Fig. 7a, b Long-range order parameter, Q, as a function of temperature for **a** ilm60 and **b** ilm65. *Solid lines* are a least-squares fit to the high-temperature data using the modified Bragg-Williams model (Eq. 11). *Dashed line* is fit by hand to the low-temperature data using the coarsening kinetic model (Eq. 17). After data collection at 500 °C in **a**, the sample was cooled to room temperature and then reheated. This causes a slight discontinuity in the kinetic relaxation curve. *Open symbols* show the cooling data

scattering vector in the refinements and no correction was made for anisotropic broadening of the superlattice reflections. This approach is only applicable once long-range order has been established in the crystal and the width of the superlattice reflections approaches those of neighbouring fundamentals. The presence of TDBs has no effect on the integrated intensity of the superlattice reflections, but the peak intensity at the Bragg position is reduced because of broadening (Warren 1990). Since only Bragg intensity is analysed in the Rietveld refinements, Q becomes a function of the average domain size. This leads to the kinetic relaxation behaviour observed during heating (see discussion).

The thermodynamics of cation ordering in this system are well described by a modified Bragg-Williams model (Harrison et al. 2000b):

$$\Delta G = \Delta H - T\Delta S_{\text{point}} \tag{7}$$

$$\Delta H = \frac{1}{2}aQ^2 + \frac{1}{4}bQ^4 \tag{8}$$

$$\Delta S_{\text{point}} = S_{\text{point}}(Q) - S_{\text{point}}(0) \tag{9}$$

$$S_{\text{point}} = -R\sum_{i,j} X_i^j \ln X_i^j \ , \tag{10}$$

where a and b are constants for a given composition. Equations (7), (8), and (9) give the excess free energy, enthalpy and configurational entropy of ordering relative to the fully disordered state at the temperature of interest. The entropy is calculated under the assumption that there is random mixing of cations on the A- and B-layers and no correlation between nearest-neighbour interlayer cation pairs (Eq. 10). This assumption overestimates the configurational entropy (and consequently the magnitudes of a and b), but does not influence the quality of fit to the experimental data (Harrison et al. 2000b). Therefore, the model may be used to define and extrapolate the equilibrium cation distribution, even when it does not provide a completely accurate description of the thermodynamic properties.

The equilibrium degree of long-range order, Q_{eq}, is found by minimising the free energy with respect to Q:

$$T = -\frac{aQ_{\text{eq}} + bQ_{\text{eq}}^3}{Rx(\ln[x + xQ_{\text{eq}}] - \ln[x - xQ_{\text{eq}}])} \ , \tag{11}$$

where x is the mole fraction of $FeTiO_3$ in the solid solution. The critical temperature is given by the limit of Eq. (11) as $Q_{\text{eq}} \to 0$:

$$T_{\text{od}} = -\frac{a}{2Rx} \ . \tag{12}$$

The solid curves in Fig. 7 are least-squares fits to the high-temperature data using Eq. (11). Only values of Q determined from diffraction patterns with sharp superlattice reflections were included in the fit. The cooling data at 200 and 400 °C in ilm60 were excluded. Values of $a = -11\,000 \pm 200$ J mol^{-1} and $b = -1100 \pm 400$ J mol^{-1} were obtained for ilm60 and $a = -12\,800 \pm 200$ J mol^{-1} and $b = -2200 \pm 600$ J mol^{-1} for ilm65, yielding $T_{\text{od}} = 830 \pm 20$ °C and $T_{\text{od}} = 911 \pm 20$ °C. These values are in good agreement with the trend established by Harrison et al. (2000a) for more ilmenite-rich compositions (Fig. 1).

Spontaneous strain

The a-cell parameter varies roughly linearly with temperature and shows little correlation with the magnetic and cation ordering transitions (Fig. 8a, b). The c cell parameter has an unusual temperature dependence, which is best visualised in terms of the spontaneous strain:

$$e_{33} = \frac{c - c_0}{c_0} \ , \tag{13}$$

where c_0 is the hypothetical cell parameter of the high-symmetry phase extrapolated to the temperature of interest (Fig. 8c, d). Values of c_0 were determined by linear extrapolation of the cell parameters measured above T_{od} to lower temperatures. The linear decrease in e_{33} between room temperature and 300 °C correlates with the magnetic ordering transition. The fact that the decrease continues until well above T_{c} is further evidence of magnetic heterogeneity in these samples. In ilm60 (Fig. 8c), e_{33} increases slightly above 300 °C and then decreases linearly to zero between 550 °C and T_{od}. Ilm65 shows a similar temperature dependence (Fig. 8d).

Discussion

Short-range ordering

The high integrated intensity of the (003) reflection in ilm60 demonstrates that a high degree of short-range order develops on quenching (Fig. 6b). Short-range order describes correlation between neighbouring cation site occupancies. Ordering in these samples is driven by the need to avoid nearest-neighbour Ti–Ti pairs, which have a high energy due to electrostatic repulsion across the shared face of the oxygen coordination octahedra (Fig. 2b). The probability of finding Ti on an A-layer next to Ti on a B-layer can be written:

$$P_{\text{Ti-Ti}}^{\text{A-B}} = X_{\text{Ti}}^{\text{A}} X_{\text{Ti}}^{\text{B}}(1 - \sigma) = X_{\text{Ti}}^2(1 - Q^2)(1 - \sigma) \ , \tag{14}$$

where σ is the short-range order parameter and X_{Ti} is the ratio of Ti cations to total cations in the system (Vinograd et al. 1997). When $\sigma = 0$ (no short-range order), $P_{\text{Ti-Ti}}^{\text{A-B}}$ is equal to the product of the concentration of Ti on the A- and B-layers. When $\sigma = 1$ (full short-range order), there is complete nearest-neighbour Ti–Ti avoidance (i.e. $P_{\text{Ti-Ti}}^{\text{A-B}} = 0$).

A visual impression of the short-range ordered structure can be obtained using a statistical simulation approach based on the cluster variation method (Vinograd and Putnis 2001). This technique provides a way of

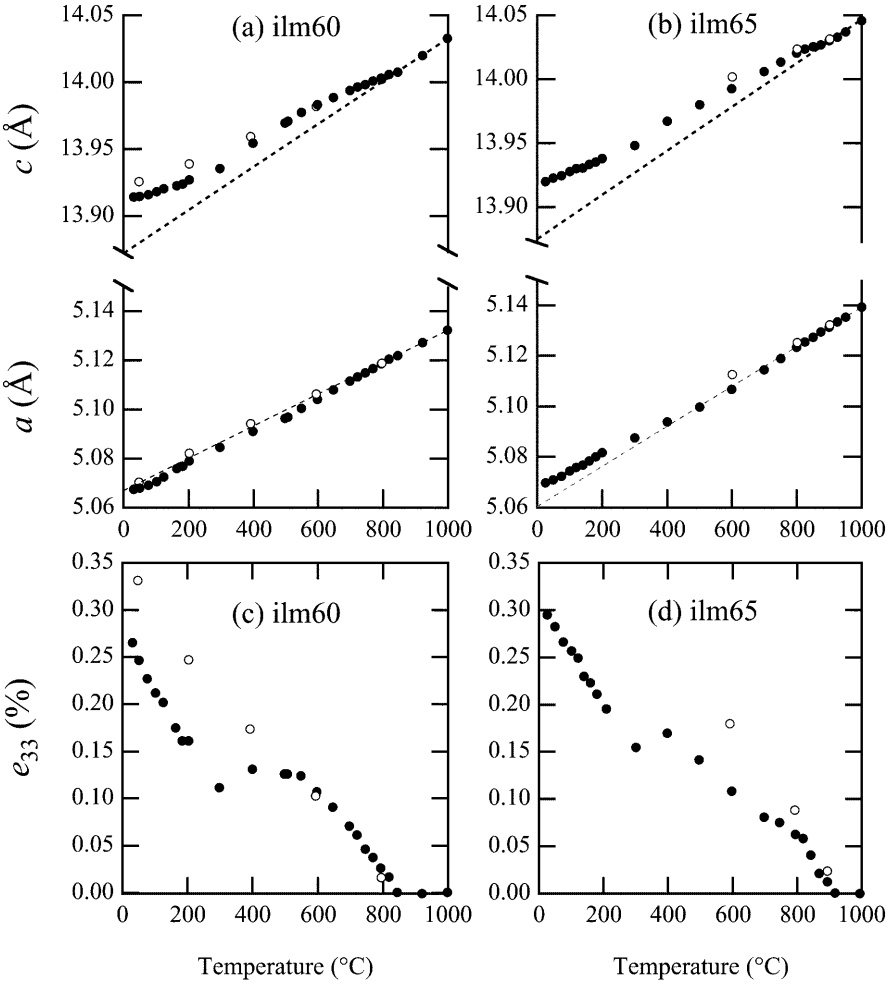

Fig. 8a–d **a** and **b** Temperature dependence of the a and c cell parameters in ilm60 and ilm65, respectively. *Dashed lines* show linear extrapolation of the data measured above T_{od}. **c** and **d** Temperature dependence of the e_{33} spontaneous strain component in ilm60 and ilm65, respectively (Eq. 13)

simulating domain structures for an arbitrary degree of short- and long-range order, and is ideally suited to the study of non-equilibrium domain structures that arise on quenching. Although the technique has so far only been applied to a square planar lattice, visualisation of the domain structures and their corresponding Fourier transforms provides a useful basis for interpreting our experimental results.

Domain structures are generated by the propagation of growth steps (Fig. 9). The conditional probability of adding an atom at site i to a preexisting growth step formed by sites j, k, l and m, is:

$$P_{\mathrm{i/jklm}} = \frac{P_{\mathrm{ijklm}}}{P_{\mathrm{jklm}}} \quad , \tag{15}$$

where i, j, k, etc. can be either Fe or Ti, and $P_{\mathrm{ijk...}}$ is the probability distribution of the given cluster of sites. For any value of X_{Ti}, Q and σ, the probability distribution of the 8-point cluster, P_{ijklmnop}, can be determined using CVM and used to derive the probability distributions of the subclusters, P_{ijklm} and P_{jklm} (Vinograd and Putnis 1999). Given a suitable starting step, the lattice can be grown atom by atom by adding Fe or Ti cations according to their conditional probabilities.

The result of a simulation with $X_{\mathrm{Ti}} = 0.3$, $Q = 0$, and $\sigma = 1$ (i.e. bulk composition ilm60 with no long-range order and full short-range order) is shown in Fig. 10a. Each site is shaded according to its occupancy and its sublattice. All Ti sites are surrounded by Fe nearest-neighbours, leading to the formation of fine-scale

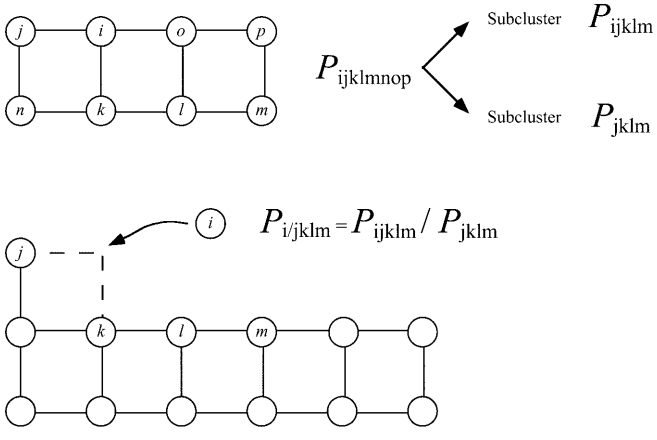

Fig. 9 Definition of clusters and subclusters used to generate domain structures. (After Vinograd and Putnis 2001)

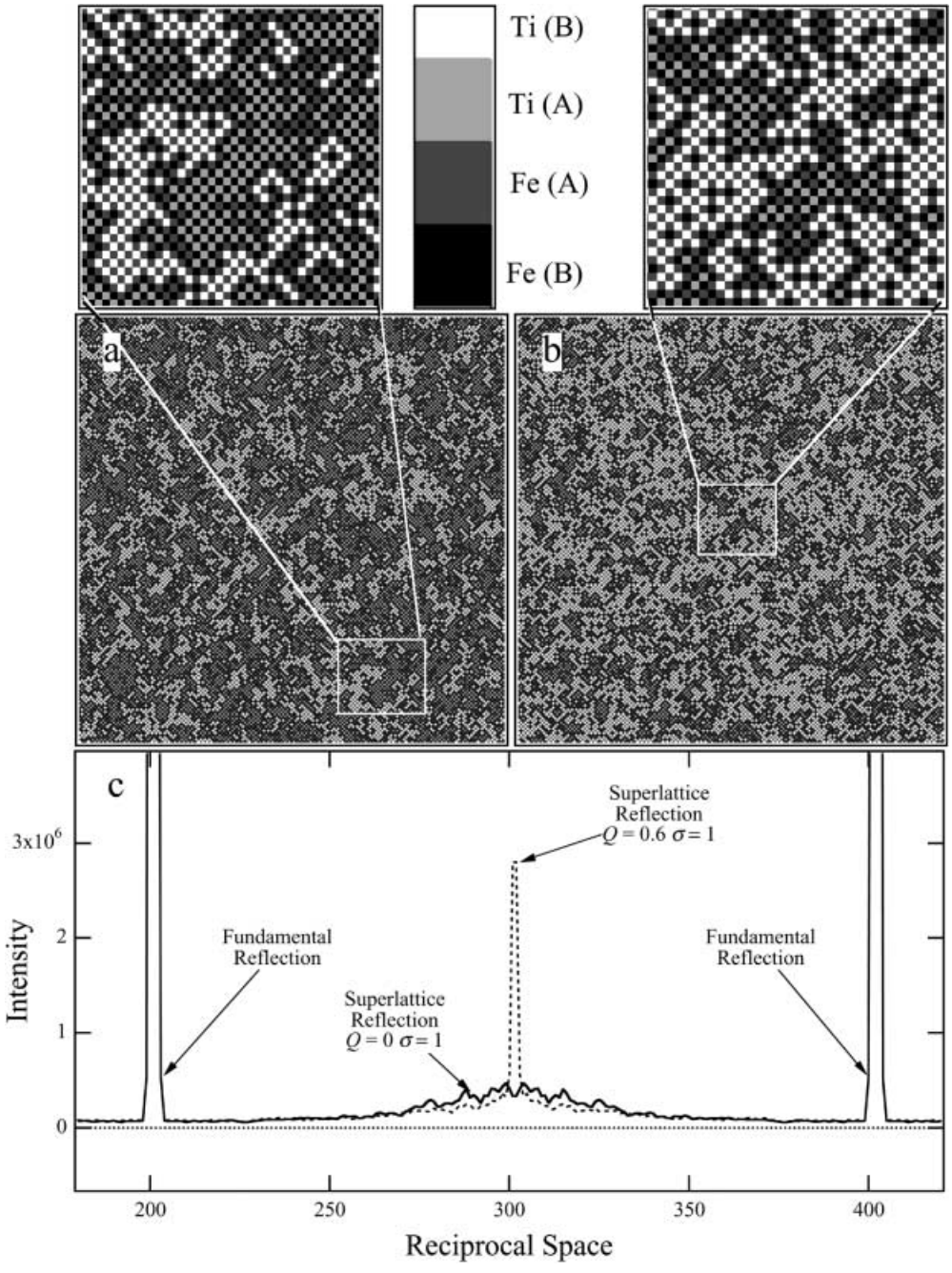

Fig. 10a–c **a** Statistical simulation of short-range order in a square planar lattice with bulk composition equivalent to ilm60 ($X_{Ti} = 0.3$, $Q = 0$, and $\sigma = 1$). *Squares* are shaded according to their occupancy and sublattice (Fe on A *dark grey*; Ti on B *white*; Fe on B *black*; Ti on A *light grey*). **b** Statistical simulation of partial long-range order, high short-range order ($X_{Ti} = 0.3$, $Q = 0.6$, and $\sigma = 1$). **c** Diffraction patterns derived from **a** (*solid line*) and **b** (*dashed line*) via fast Fourier transform

ordered and antiordered domains. Due to the choice of shading, ordered domains appear as a white on a dark grey chessboard pattern, while antiordered domains appear as light grey on black. The domains are surrounded by disordered Fe-rich TDBs, which appear dark grey on black. Fe-enrichment of the TDBs is a natural consequence of short-range ordering, since the only way to achieve complete Ti–Ti avoidance is to move Ti away from the disordered boundaries and into the domains. The domains themselves become enriched in Ti relative to the bulk composition. In the limiting case (i.e. when the domains are infinitely small), the Fe:Ti ratio within the domains approaches 1:1 and the TDBs contain only Fe. This is not quite the case in Fig. 10a, since each ordered domain can be seen to contain a significant number of excess Fe defects (although a lower number on average than in the long-range ordered structure with this bulk composition). A simulation with $X_{Ti} = 0.3$, $Q = 0.6$ and $\sigma = 1$ is shown in Fig. 10b. This illustrates a possible non-equilibrium domain structure that would be obtained during the transformation from short- to long-range order. Here, the general structure of ordered and antiordered domains is retained, but the volume fraction of ordered domains is greater.

Diffraction patterns of the short- and long-range ordered structures were obtained by performing a fast

Fourier transform (FFT) of the 201×201 matrix of Fe and Ti cations (Fig. 10c). To eliminate termination effects, the matrix was multiplied by a raised cosine function, which falls smoothly to zero at the edge of the box. The profiles in Fig. 10c were then obtained by projecting the diffraction pattern along y^*. Long-range ordering produces a sharp superlattice reflection superimposed on a diffuse background (dashed curve). Short-range ordering produces a highly diffuse reflection superimposed on a gently curving background. The integrated intensity is equal in both cases. The width of the short-range ordered reflection yields an average domain size of four to five nearest-neighbour distances. This is comparable with the broadening of the (003) reflection in ilm60, which suggests a domain size of 20 Å, or six to seven nearest-neighbour distances.

The main difference between the square lattice simulations and our experimental results is that short-range ordering in ilmenite–hematite is highly one-dimensional, with ordering fluctuations constrained almost entirely to **k**-vectors parallel to [003]*. A simplified domain model for a bulk composition of ilm67 (containing equal proportions of Fe^{2+}, Fe^{3+} and Ti) is presented in Fig. 11. The model consists of ordered and antiordered ilmenite-like domains surrounded by hematite-like TDBs, with a domain size approximately equal to the c cell parameter (14 Å). Horizontal lines correspond to the (003) planes. Cations lying on the (003) planes belong to the A sublattice, whereas those lying halfway between belong to the B sublattice. As the domain size approaches the unit-cell dimensions, the cation occupancy of adjacent layers remains highly correlated, leading to a diffuse (003) reflection with a high integrated intensity (Fig. 6b). The diagonal lines in Fig. 11 show the $(0\bar{1}1)$ planes. There is no short-range correlation between adjacent planes, leading to the low integrated intensity of the $(0\bar{1}1)$ reflection (Fig. 6a). This loss of intensity is balanced by an increase in background scattering around the $(0\bar{1}1)$ reflection. This background may be wrongly attributed to the (003) reflection in the powder diffraction experiment, since there is significant overlap between the peaks. This may explain why the (003) reflection has a much higher integrated intensity than expected for this bulk composition (i.e. higher than the dashed line in Fig. 6b).

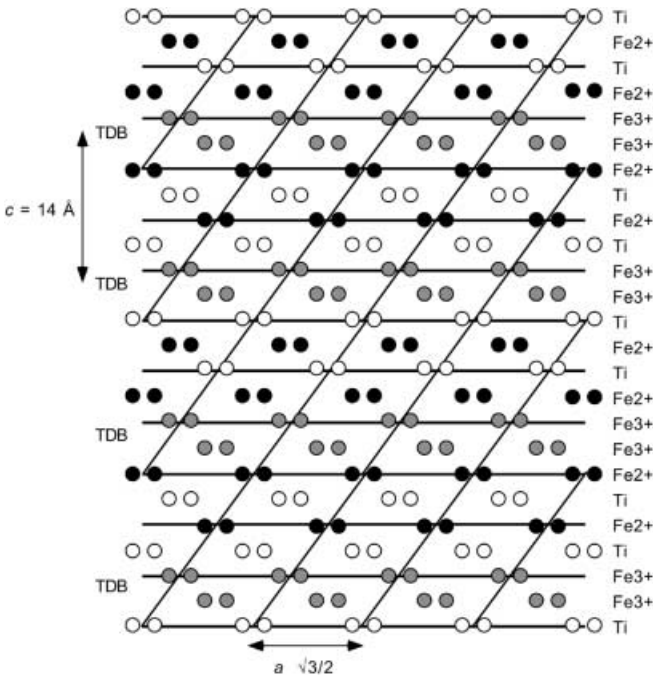

Fig. 11 Schematic representation of the ilmenite structure viewed down the a-axis, showing the possible short-range ordered structure in a quenched sample with bulk composition ilm67 (Fe^{2+} *black*; Fe^{3+} *grey*; Ti *white*). *Horizontal lines* show the trace of the (003) planes, *diagonal lines* show the trace of the $(0\bar{1}1)$ planes

Transformation from short- to long-range order

The order parameter shows a pronounced kinetic relaxation on heating (Fig. 7). This phenomenon is normally described using a macroscopic rate law, whereby the rate of ordering is proportional to the thermodynamic driving force (i.e. $dQ/dt \propto dG/dQ$; Harrison et al. 1998; Redfern et al. 1999). Equilibrium is defined by $dG/dQ = 0$, so in a constant heating rate experiment the maximum in the kinetic curve occurs just after it crosses the equilibrium curve. The kinetic relaxation in these experiments is unusual because the maximum occurs well before the equilibrium curve is reached. The origin of this behaviour may be demonstrated using a simple coarsening model.

As demonstrated by the statistical simulations in Fig. 10, the transformation from short- to long-range order occurs at the atomic scale via the growth of very fine-scale ordered domains at the expense of antiordered domains (or vice versa). At any point in time, the degree of long-range order is given by:

$$Q = N^+ Q_{eq} - N^- Q_{eq} \ , \qquad (16)$$

where N^+ and N^- are the fractions of ordered and antiordered domains ($N^- = 1 - N^+$). Growth of the ordered domains is expected to follow a power law of the form $N^+ \propto (t/\tau)^m$, where t is time and $\tau^{-1} = \gamma \exp(-E_a/RT)$. Growth slows down as the ordered regions coalesce and equilibrium is reached. This can be modelled using the Avrami equation (Malcherek et al. 1997):

$$N^+ = N_0^+ + (1 - N_0^+)\left(1 - e^{-(t/\tau)^m}\right) \ , \qquad (17)$$

where N_0^+ is the initial fraction of ordered domains. A constant heating rate can be approximated by a series of isothermal annealing steps. The value of N^+ at the end of each annealing step is calculated from Eq. (17) and taken as the starting value for the subsequent step at a higher temperature.

Results of the coarsening model are shown as the dashed lines in Fig. 7. It is not possible to determine γ and E_a independently from a constant heating rate experiment. Therefore, an arbitrary value of $E_a = 300$ kJ mol^{-1} was assumed and γ and m were adjusted by trail and error to give the best observed fit

to the experimental data. Values of $\gamma = 10^{-4}$ s^{-1} and $m = 0.1$ were used for both ilm60 and ilm65. Heating rates of 0.6 and 1.5 K min^{-1} were used for ilm60 and ilm65, respectively, consistent with the known thermal history of the samples. Ignoring the data point at 200 °C in ilm60 (which is probably influenced by magnetic ordering), the coarsening model provides an excellent description of the kinetic relaxation behaviour. Relaxation is determined by the balance between the rate of coarsening and the rate of disordering within the domains. The maximum in the kinetic curve occurs when these two rates are equal, and need not coincide with the equilibrium curve.

Magnetic heterogeneity

On the basis of these experiments alone, it is only possible to speculate about the origin of the magnetic heterogeneity seen in Fig. 4. The value of T_c is controlled on a mesoscopic length scale by factors such as the composition, cation distribution and stoichiometry. Our own (unpublished) experiments on these samples indicate that the intrinsic correlation between cation distribution and T_c is negligible in comparison to the effects of bulk composition and non-stoichiometry. The relationship between bulk composition and T_c is well defined (Fig. 1). The effect of non-stoichiometry depends on the temperature at which it is acquired. The stability field of ilmenite–hematite has a finite width at high temperatures (Lindsley 1991). It is possible to synthesise slightly oxidised single-phase material at 1300 °C and retain the non-stoichiometry on quenching. Nord and Lawson (1992) cite unpublished experiments which show that T_c is lower in the non-stoichiometric phase. This does not then explain the anomalously high T_c observed in these samples. At lower temperatures, the stability field of ilmenite–hematite is very narrow. Under these conditions, slight oxidation produces small amounts of Ti-rich pseudobrookite–ferropseudobrookite solid solution. The remaining ilmenite–hematite is enriched in Fe and has a higher T_c. This cannot be ruled out as a source of heterogeneity in these samples, although no traces of pseudobrookite–ferropseudobrookite were seen in any of the neutron diffraction patterns at any of the temperatures studied.

A third possibility is that the magnetic heterogeneity reflects the compositional heterogeneity associated with Fe-enrichment of TDBs. As shown in Fig. 10, statistical models predict that compositional heterogeneity exists in both the short- and long-range ordered structures on a length scale of several nearest-neighbour distances. Due to the short-range nature of magnetic interactions, it is conceivable that such local compositional heterogeneities would enhance the degree of short-range magnetic order at temperatures far above the bulk T_c. Harrison et al. (2000a, b) further speculated that compositional heterogeneity might be enhanced on cooling through the solvus if the TDBs acted as nuclei for the disordered Fe-rich phase. It is unlikely that significant exsolution occurs during the quench. However, heterogeneous nucleation at TDBs may become important as the quenched samples are heated slowly through the solvus during the neutron diffraction experiments.

Relevance to natural material

Interest in the phenomenon of self-reversed thermoremanent magnetization (SR-TRM) has been revived recently, following a series of detailed micromagnetic studies on ilmenite samples from the Nevado del Ruiz and Pinatubo dacitic pumices (Haag et al. 1993; Hoffmann 1996; Hoffmann and Fehr 1996; Bina et al. 1999). Ilmenite–hematite grains from these volcanoes are zoned, with the rims being slightly Fe-richer than the cores. The chemical zonation is thought to be caused by the injection of a more basaltic magma into the dacitic magma chamber shortly before eruption. Despite the small difference in composition between the rim and the core (rim = ilm53–ilm57, core = ilm58), their magnetic properties are very different. The rim is antiferromagnetic with a weak parasitic moment, while the core is strongly ferrimagnetic. Hoffmann and Fehr (1996) suggested that the Fe-rich rim of these grains acts as the so-called *x*-phase, which is responsible for the SR-TRM acquired after eruption.

This study provides some insight into the possible structural and microstructural state of these rapidly cooled natural samples. The antiferromagnetic nature of the rim phase suggests that it grew within the disordered $R\bar{3}c$ stability field and was quenched fast enough on eruption to prevent long-range cation ordering. We would expect the rim to have a high degree of short-range cation order, similar to that observed in our quenched ilm60 sample. The ferrimagnetic nature of the core phase suggests that it either grew within the ordered $R\bar{3}$ stability field or cooled at a much slower rate, allowing time for cation ordering to take place after eruption. In the first case, we would expect the core to have no TDBs, since these would have been annealed out before eruption. In the latter case, we would expect the core to contain fine-scale twin domains, such as those observed in our slowly cooled synthetic samples (i.e. domain size < 400 Å). At present, no TEM study has been performed to determine which of these scenarios is correct. Micromagnetic studies show that the cores contain many free-standing magnetic walls, which move easily through the crystal. This suggests that no TDBs are present, since these would strongly pin the magnetic walls (Nord and Lawson 1992; Harrison 2000). This puts a strict constraint on the temperature of the magma before eruption, since the compositions of the core and rim must straddle the $R\bar{3}c$ to $R\bar{3}$ phase boundary. Assuming compositions of ilm58 and ilm53 for the core and rim, respectively, the temperature before eruption is constrained to lie between 700 and 790 °C (Fig. 1).

The changes in structure and microstructure which occur as a function of distance from the rim to the core will be equivalent to those which occur as a function of temperature during heating of our quenched samples. The mechanism of the short- to long-range order transformation, and the microstructures which are produced along the way, are sure to play a crucial role in the self-reversal process. The experimental observations and statistical simulations presented in this study provide the first step towards understanding this phenomenon. Further work will concentrate on developing methods for simulating non-equilibrium domains structures in three-dimensional systems with the ilmenite topology.

Acknowledgements The authors would like to thank Victor Vinograd for providing Fig. 10a and b, and for his invaluable discussions regarding the nature of short-range order. We would also like to thank Winfried Kockelmann for his assistance in performing the neutron diffraction experiments. R.J.H. acknowledges the support of the Marie Curie Fellowship.

References

Bina M, Tanguy JC, Hoffmann V, Prevot M, Listanco EL, Keller R, Fehr KT, Goguitchaichvili AT, Punongbayan RS (1999) A detailed magnetic and mineralogical study of self-reversed dacitic pumices from the 1991 Pinatubo eruption (Philippines). Geophys J Int 138: 159–178

Brown NE, Navrotsky A, Nord GL, Banerjee SK (1993) Hematite (Fe_2O_3)-ilmenite ($FeTiO_3$) solid solutions: determinations of Fe-Ti order from magnetic properties. Am Mineral 78: 941–951

Deines P, Nafziger RH, Ulmer GC, Woermann E (1974) Temperature-oxygen fugacity tables for selected gas mixtures in the system C–H–O at one atmosphere total pressure. Pennsylvania State University, College of Earth and Mineral Sciences. Bull Exp Stn 88: 129

Delhez R, de Keijser TH, Langford JI, Louër D, Mittemeijer EJ, Sonneveld E (1995) Crystal imperfection broadening and peak shape in the Rietveld method. In: Young RA (ed) The Rietveld method. Oxford University Press, New York

Dzyaloshinsky I (1958) A thermodynamic theory of "weak" ferromagnetism of antiferromagnetics. J Phys Chem Solids 4: 241–255

Ghiorso MS (1997) Thermodynamic analysis of the effect of magnetic ordering on miscibility gaps in the FeTi cubic and rhombohedral oxide minerals and the FeTi oxide geothermometer. Phys Chem Miner 25: 28–38

Haag M, Heller F, Lutz M, Reusser E (1993) Domain observations of the magnetic phases in volcanics with self-reversed magnetization. Geophys Res Lett 20: 675–678.

Harrison RJ (2000) Magnetic transition in minerals. In: Transformation processes in minerals. Rev Mineral Mineral Soc Am 40 (in press)

Harrison RJ, Putnis A (1999) Determination of the mechanism of cation ordering in magnesioferrite ($MgFe_2O_4$) from the time- and temperature-dependence of magnetic susceptibility. Phys Chem Miner 26: 322–332

Harrison RJ, Redfern SAT, O'Neill HSC (1998) The temperature dependence of the cation distribution in synthetic hercynite ($FeAl_2O_4$) from in-situ neutron diffraction. Am Mineral 83: 1092–1099

Harrison RJ, Redfern SAT, Smith RI (2000a) In-situ study of the R-3 to R-3c phase transition in the ilmenite-hematite solid solution using time-of-flight neutron powder diffraction. Am Mineral 85: 194–205

Harrison RJ, Becker U, Redfern SAT (2000b) Thermodynamics of the R-3 to R-3c phase transition in the ilmenite-hematite solid solution. Am Mineral 85: 1694–1705

Hoffman KA (1992) Self-Reversal of thermoremanent magnetization in the ilmenite–hematite system: order-disorder, symmetry, and spin alignment. J Geophys Res 97: 10883–10895

Hoffmann V (1996) Experimenteller Mikromagnetismus zur Aufklärung der physikalischen Prozesse des Erwerbs und der Stabilität von Daten des Paläo-Magnetfeldes der Erde. Habilitation Thesis, Munich

Hoffmann V, Fehr KT (1996) Micromagnetic, rockmagnetic and minerological studies on dacitic pumice from the Pinatubo eruption (1991, Philippines) showing self-reversed TRM. Geophys Res Lett 23: 2835–2838

Holland TJB, Redfern SAT (1997) Unit cell refinement from powder diffraction data: the use of regression diagnostics. Mineral Mag 61: 65–77

Ishikawa Y, Saito N, Arai M, Watanabe Y, Takei H (1985) A new oxide spin glass system of (1-x)$FeTiO_3$–xFe_2O_3. I. Magnetic properties. J Phys Soc Jpn 54: 312–325

Larson AC, Von Dreele RB (1994) GSAS general structure analysis system. LANSCE MS-H805. Los Alamos National Laboratory, Los Alamos, NM 87545, USA

Lindsley DH (1991) Experimental studies of oxide minerals. In: Oxide minerals. Rev Mineral Am Mineral Soc 25: 69–106

Malcherek T, Salje EKH, Kroll H (1997) A phenomenological approach to ordering kinetics for partially conserved order parameters. J Phys Cond Matt 9: 8075–8084

Marais S, Salje EKH (1991) Derivation of a rate law for non-uniform systems and continuous order parameters. J Phys Cond Matter 3667–3670

Nord GL, Lawson CA (1989) Order-disorder transition-induced twin domains and magnetic properties in ilmenite-hematite. Am. Mineral 74: 160

Nord GL, Lawson CA (1992) Magnetic properties of ilmenite70-hematite30: effect of transformation-induced twin boundaries. J Geophys Res 97(B): 10897

Redfern SAT, Harrison RJ, O'Neill HSC, Wood DRR (1999) Thermodynamics and kinetics of cation ordering in $MgAl_2O_4$ spinel up to 1600 °C from in situ neutron diffraction. Am Mineral 84: 299–310

Shirane G, Pickart SJ, Nathans R, Ishikawa Y (1959) Neutron-diffraction study of antiferromagnetic $FeTiO_3$ and its solid solutions with α-Fe_2O_3. J Phys Chem Solids 10: 35–43

Shirane G, Cox DE, Takei WJ, Ruby SL (1962) A study of the magnetic properties of the $FeTiO_3$-Fe_2O_3 system by neutron diffraction and the Mössbauer effect. J Phys Soc Jpn 17: 1598–1611

Uyeda S (1958) Thermo-remanent magnetism as a medium of palaeomagnetism, with special reference to reverse thermo-remanent magnetism. Jpn J Geophys 2: 1–123

Vinograd VL, Putnis A (1999) The description of Al, Si ordering in aluminosilicates using the cluster variation method. Am Mineral 84: 311–324

Vinograd VL, Putnis A (2001) A two-dimensional spin model of Al/Si order in feldspars: visualisation of short-range and long-range ordering. Eur J Mineral 13: 273–288

Vinograd V, Saxena SK, Putnis A (1997) Calculation of the probability distribution of basic clusters involved in cluster-variation approximations to the Ising model. Phys Rev (B) 56: 11493–11502

Warren BE (1990) X-ray diffraction. Dover, New York